

Plasma enhanced layer-by-layer deposition and nanocrystallization of hydrogenated amorphous silicon films

Zhuo Chen,^{a)} John A. Mucha, Vincent M. Donnelly,^{b)} and Demetre J. Economou^{c)}
*Plasma Processing Laboratory, Department of Chemical and Biomolecular Engineering,
University of Houston, Houston, TX 77204-4004*

(Received 27 June 2013; accepted 11 October 2013; published 5 November 2013)

A layer-by-layer technique, using a reactor with two separate plasma sources, was developed for a-Si:H deposition and nanocrystallization. Substrates were heated to 250 °C and rotated between the two plasma sources, with selectable residence times in each source. A SiH₄/He/H₂ capacitively coupled plasma (CCP) was employed to deposit a thin a-Si:H layer that was subsequently exposed to a H₂ inductively coupled plasma (ICP) to induce crystallization in the layer. The cycle of deposition followed by nanocrystallization was repeated to grow thin films with different volume fractions (from 0% to 72%) of crystalline material, as determined by Raman spectroscopy. For the same *total* exposure time in the CCP, many short exposures (i.e., more cycles) were more effective in producing nanocrystalline Si compared to few long exposures. In addition, for a given number of cycles, the fraction of nanocrystalline Si increased with increasing ICP-to-CCP exposure time ratio (which ranged from 1/4 to 4/1). Transmission electron microscopy revealed crystallites with columnar structure along the film growth direction. Mass spectrometric monitoring of a dominant reaction product emanating from films grown in the CCP and subsequently exposed to a D₂ ICP suggested that etching and structural reorganization during nanocrystallization occurred throughout the film volume. © 2013 American Vacuum Society. [<http://dx.doi.org/10.1116/1.4827258>]

I. INTRODUCTION

Due to their great potential for economic production of electric power from solar energy, photovoltaics (PV), though studied and utilized for more than 30 years, continue to be an area of intense activity.^{1,2} Single crystal Si and polycrystalline Si with high efficiency (exceeding 25%) dominate the PV industry today.³ To obtain high efficiency, these solar cells need to be thick, reasonably high quality Si,⁴ resulting in high manufacturing costs. Thin films of hydrogenated amorphous Si (a-Si:H) are a low cost alternative, due to cheaper manufacturing and high optical absorption coefficient compared to crystalline Si.⁵ These films contain ~10–15% hydrogen that passivates Si dangling bond defects, resulting in a decrease in the carrier recombination rate and thus practical efficiencies of up to 12%.¹ However, a-Si:H films suffer from stability issues. After the first few hundred hours of exposure to sunlight, the efficiency of the cell drops. This so-called Staebler–Wronski effect⁶ can be minimized by inducing the formation of microcrystalline Si ($\mu\text{c-Si}$) or nanocrystalline Si (nc-Si) in the a-Si:H film.^{1,7–9} For example, by using a hydrogen-rich deposition process, large quantities of atomic hydrogen arrive at the growing surface, promoting the formation of a fine grain (~30–500 Å) nanocrystalline Si embedded in the otherwise amorphous matrix.¹⁰ nc-Si films with crystalline volume fraction in the range of 40–60% appear to have the best efficiency both initially and after exposure to light.⁹ It follows that control of the crystalline volume fraction in nc-Si films plays an important role for the performance of solar cells based on this material.

Matsuda and coworkers used a H₂/SiH₄ capacitively coupled plasma (CCP) to grow microcrystalline silicon.¹¹ They found that the crystalline volume fraction increased with substrate temperature, went through a maximum of 40% at ~400 °C, and then decreased for higher temperatures up to 500 °C. Aydil, Maroudas, and co-workers performed molecular dynamics simulations^{12,13} and attenuated total reflection Fourier transform infrared (FTIR) absorption spectroscopy measurements to study growth and crystallization of a-Si:H films. They found that the film surface was mostly covered with monohydrides and some trihydrides, while the bulk contained SiH, SiH₂, and SiH₃. When nc-Si:H formed, more dangling bonds were created on the growth surface by abstraction reactions of H, which enhanced decomposition of higher hydrides into monohydrides. Parsons *et al.*¹⁴ grew thin layers of a-Si:H in a SiH₄ CCP, then exposed the film to a H₂ plasma in the same reactor. No deposits were observed when the H₂ exposure time exceeded 2.8 times the deposition time. Eighteen SiH₄/H₂ cycles were required to initiate film growth on SiO₂ (only a few cycles were required on Si substrates). Using D₂ instead of H₂ and mass spectrometric analysis of the layer-by-layer (LbL) growth, they observed that hydrogen was removed from a-Si:H by D-atom abstraction in the D₂ plasma to form hydrogen deuteride (HD), and to a lesser extent, through etching reactions that generated deuterio-silanes. Drevillon and co-workers¹⁵ used *in-situ* spectroscopic ellipsometry and postdeposition Raman analysis to explore the relative exposure times of deposition (time t_1) versus H₂-exposure (time t_2) and found regions of a-Si, $\mu\text{c-Si}$, and no-film growth for t_1 ranging from 8 s to 40 s and t_2/t_1 from 0 to 2.5. The following approximate t_2/t_1 regions were identified: $t_2/t_1 < 0.5$ resulted in a-Si:H deposition, t_2/t_1 in the range of 0.8 to ~1.7 resulted in $\mu\text{c-Si}$ deposition, and

^{a)}Present address: Micron, Boise, Idaho.

^{b)}Electronic mail: vmdonnelly@uh.edu

^{c)}Electronic mail: economou@uh.edu

$t_2/t_1 > 1.7$ yielded no deposition. Shimizu and co-workers¹⁶ used *in-situ* spectroscopic ellipsometry to study LbL growth on several substrates by alternating pure SiH₄ (or highly dilute ~2% SiH₄/H₂) plasma with H₂ plasma exposures. The results suggested that the 40 Å surface roughness layer (a-Si/nc-Si/voids = 20/30/50) was present under conditions that promoted microcrystallinity. Although insightful, the above studies used a common reaction chamber for LbL, and there is a distinct possibility for cross contamination or wall-effects within each cycle.

To alleviate this concern, Asano¹⁷ introduced sample rotation between physically separate plasma regions in a common vacuum chamber to deposit and crystallize a-Si:H films using a LbL approach. Asano used sealing rings and pressure differentials (0.6 Torr deposition and 0.85 Torr H₂ exposure) between the subchambers in the vacuum vessel to minimize cross-contamination. He found that at 250 °C, chemical etching was not significant, since the deposited layer thickness was nearly constant after either 6 s or 48 s per cycle exposure to the H₂ plasma. In addition, the crystalline volume fraction increased with H₂ discharge power density. He proposed that H atoms in the H₂ plasma chemisorb and decrease the reactivity of the surface toward SiH_x, increasing its diffusion length and mobility, which leads to the formation of μ c-Si.¹⁷ Similarly, Roca i Cabarrocas and co-workers¹⁸ introduced a multiplasma system capable of *in-vacuo* sample rotation. However, in some of their more definitive studies,^{19,20} it is unclear whether sample rotation between deposition and crystallization was employed since waiting periods¹⁹ were held between the two processes. Nevertheless, this group established a phase diagram for LbL processing that included regions of a-Si:H growth ($t_2/t_1 < \sim 2$), μ c-Si growth ($t_2/t_1 \sim 2-6$), and no-film deposition ($t_2/t_1 > \sim 6$).

More recently, Roca i Cabarrocas *et al.*²¹ proposed that nanocrystalline silicon particles formed during plasma enhanced chemical vapor deposition (PECVD) using SiH₄ and H₂ are the main building blocks of epitaxial Si growth at 175 °C on c-Si (100) substrates. Johnson *et al.*²² applied tailored voltage waveforms to decouple the ion bombardment energy from the power input to a CCP PECVD reactor, which allowed growth of quality μ c-Si:H films at a reasonable rate of 3 Å/s. Senouci *et al.*,²³ studied the influence of H atoms on the transition from amorphous to nanocrystalline films grown by reactive rf magnetron sputtering. They proposed a conceptual model of the initial stages of nanocrystallization. Finally, Yan *et al.*²⁴ discussed photovoltaic applications of amorphous and nanocrystalline silicon thin films on flexible substrates.

In the present work, layer-by-layer deposition and nanocrystallization of a-Si:H films was studied using a novel reactor with rotating substrates and two distinct stationary plasma sources within a single vacuum chamber. Films were grown by PECVD in a silane-containing CCP, and then crystallized in a hydrogen inductively coupled plasma (ICP), in a cyclic process. Unique features of this reactor were: (1) rotation of the sample between the two plasma sources without extinguishing either plasma, (2) variable process time in each plasma, (3) minimal cross-contamination during the

process, and (4) H₂ ICP (instead of CCP) to provide a higher number density of H atoms for nanocrystallization. The total deposited material was held relatively constant but the number of deposition-crystallization cycles was varied, along with the deposition-to-crystallization time ratio. Raman spectroscopy, transmission electron microscopy (TEM), spectroscopic ellipsometry (SE), and transmission FTIR spectroscopy were used for film characterization. Etching during exposure of films to a D₂ ICP was monitored by mass spectrometry. A simple mathematical model of diffusion-controlled etching during this step was formulated, and model results were compared with experiments.

II. EXPERIMENTAL APPARATUS

Figure 1 shows a schematic of the experimental apparatus. It consisted of two stationary plasma sources in a vacuum chamber. The CCP source was fed through a showerhead electrode with a mixture of 100 sccm 1% SiH₄ diluted in He and 40 sccm H₂, to grow a-Si:H films. The ICP source was fed with 80 sccm H₂ to crystallize the films. The total pressure in the vacuum chamber was 720 mTorr. Based on the size of the gap through which gas exited the plasma volumes and the gas flow rates used, only a negligible pressure drop is expected between the plasmas and the main vacuum chamber. For most experiments, 4 in. diameter aluminum substrate holders were mounted in cut-out wells in a grounded aluminum susceptor, which could be rotated by a motor located outside the vacuum chamber. Glass substrates (1 in. diameter Schott D263M) were mounted on the substrate holders upside down facing the plasma and were heated to 250 °C by radiation emanating from resistive heaters on the back of the substrate holders. The heating elements were purged with Ar gas to minimize deposition on their surface. In mass spectrometer experiments, used to study the product evolution during exposure of the deposited a-Si:H film to a deuterium ICP, a 4 in. diameter Si substrate was used.

The SiH₄/He/H₂ CCP was formed between the grounded substrate holder and the 4 in. diameter showerhead electrode

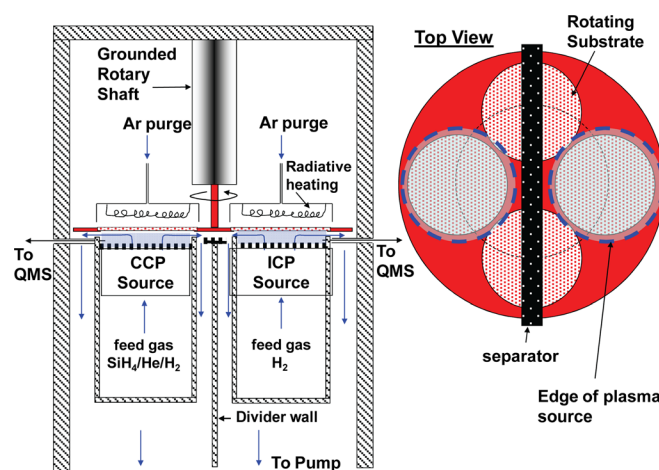


Fig. 1. (Color online) Schematic of the dual plasma source reactor with rotating susceptor. Gas flow through the plasma sources is indicated by blue arrows. CCP = capacitively coupled plasma, ICP = inductively coupled plasma.

20 mm apart. Radio frequency (rf) power at 13.56 MHz was applied to the electrode by a function generator (Hewlett Packard model 3325A) and rf amplifier (ENI model A-150) through a matching network. The power density was fixed at 0.33 W/cm^2 (based on the rf electrode area) for all experiments. A cylindrical quartz tube was used to radially confine the plasma. Additional confinement was obtained with 14 NdFeB permanent magnets ($\sim 10\,000$ Gauss) placed azimuthally outside the quartz tube with alternating poles. A 2 mm vertical gap between the substrate and the edge of the quartz tube provided enough space for gas pumping. The geometry did not allow Langmuir probe measurements to be performed. Under these conditions, a plasma density of $\sim 10^{10} \text{ cm}^{-3}$ is expected, with a broad distribution of low ion bombardment energies ($\sim 10 \text{ eV}$) because of the highly collisional conditions in the plasma sheath. It should be noted that, under our experimental conditions, the film deposited in the CCP was always amorphous. Furthermore, crystallization in the ICP occurred throughout the film volume (see below). Thus, ion bombardment (which is limited to the surface) is not as critical under our conditions.

The ICP was sustained by a 3-turn flat spiral water-cooled coil under a 4 in. diameter alumina disk. A focus ring confined the plasma radially. The gap between the alumina disk and the substrate was 20 mm. 170 W of power was supplied at 29 MHz by a function generator (Hewlett Packard model 8656B) and rf power amplifier (ENI model A-300) through a matching network. Again, it was not possible to carry out Langmuir probe measurements. Under the ICP conditions used, a plasma density of $\sim 10^{11}/\text{cm}^3$ is expected. Due to the much higher electron density, the H number density is expected to be roughly an order of magnitude higher than in the CCP. Using a spectrometer described previously,²⁵ optical emission from H-Balmer alpha and the 750.4 nm line of Ar (10% Ar was added in a few experiments) was recorded. With a H-to-Ar emission ratio of 0.4 (corrected for spectrometer response), the procedure outlined in a prior publication²⁶ was used to estimate a H-atom density of $4 \times 10^{14} \text{ cm}^{-3}$ in the ICP at 170 W and 720 mTorr, assuming a temperature of 500 K, or roughly 2% dissociation of H_2 .

Upon susceptor rotation, the central axis of the ICP described the same circle as that of the CCP and the center of the substrates. Note that when one substrate was in the CCP, the diametrically opposite substrate was in the ICP. One cycle of the process consisted of bringing a substrate over the CCP, where deposition occurred for time t_1 (ranging from 5 s to 40 min), and then rotating the substrate over to the ICP to induce nanocrystallization for time t_2 . The ratio of t_2/t_1 ranged from 1/4 to 4/1. Deposition and crystallization were repeated for n_c number of cycles. Both plasmas remained ignited for the duration of the process, including during sample movement. Three main groups of experiments (1, 10, or 120 cycles, respectively) were performed with stopped rotation to study nanocrystallization with different ICP to CCP process time ratios. In addition, experiments with 480 cycles ($t_2/t_1 = 5 \text{ s}/5 \text{ s}$) and continuous rotation (4500 cycles, $t_2/t_1 = 1.6 \text{ s}/1.6 \text{ s}$) were performed.

A mass spectrometer (UTI model 100C) was employed to monitor reaction byproducts during nanocrystallization in the ICP reactor (Fig. 2). The ICP was sampled through a pin-hole on the closed end of a $1/4$ in. diameter stainless steel tube. The mass spectrometer was used in conjunction with an intermediate chamber for reducing the sampling pressure, allowing the pressure in the mass spectrometer chamber to be $\sim 5 \times 10^{-7}$ Torr for a process pressure of 720 mTorr. Only stable products were detected with this configuration.

Raman spectra of processed films were measured in a backward scattering configuration using a T64000 (Horiba Jobin-Yvon) spectrometer equipped with a microscope ($100\times$ or $50\times$ objective) and liquid-nitrogen-cooled CCD detector. The excitation source was a 515 nm Ar^+ laser. The laser power was kept below 5 mW to avoid local heating. A spectroscopic ellipsometer (M-2000L, J. A. Woollam Co.) was also used to characterize the films. Polarized light from a xenon arc lamp, in the 250–900 nm wavelength range, was directed onto the film surface at 55° angle of incidence. Other details for these characterization methods are given below. A few films were also characterized by FTIR spectroscopy.

Cross-sectional high resolution transmission electron microscopy (HRTEM) was performed with a JEOL model JEM-2010F TEM. Dark-field images were used to investigate the detailed film microstructure of selected films. The TEM images were recorded using a standard high angle annular dark field detector. The incidence angle of the electron probe was optimized for Si (111) diffraction with the bright regions corresponding to the crystalline material. The surface of the film was coated with a sputtered Au-Pd layer to prevent charging during sample preparation using a focused ion beam (FIB).

III. RESULTS AND DISCUSSION

A. Spectroscopic ellipsometry

The SE data (Ψ and Δ) were recorded at a 55° angle of incidence and analyzed using Woollam WVASE32 software²⁷

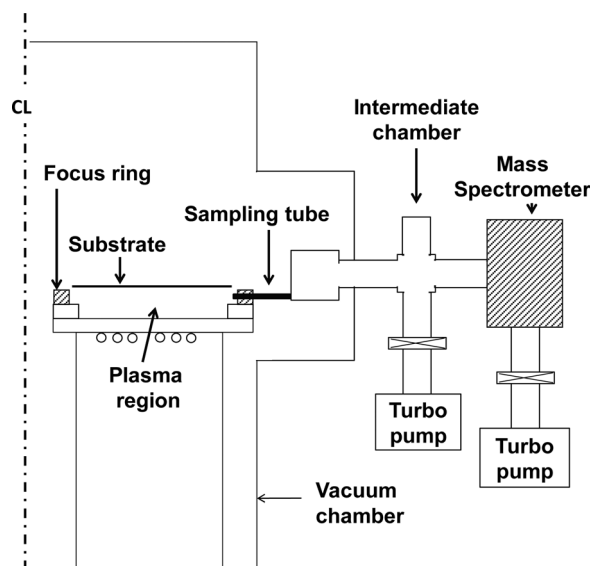


Fig. 2. Schematic of mass spectrometer sampling of the inductively coupled plasma source. Only stable species can be detected in this configuration.

to obtain film characteristics such as thickness and voids content.^{28,29} A simple three-layer model consisting of a surface (roughness) layer, a Bruggeman effective medium approximation (BEMA) layer, and substrate was used for data analysis. The BEMA layer that defined the film consisted of thickness and component fractions of a Cody–Lorentz (C-L) oscillator layer,²⁸ voids, and crystal silicon (c-Si) as adjustable (fit) parameters. Prior to depositing films, ellipsometric data were collected to obtain optical constants for the glass substrates. Inclusion of an interface layer between the glass substrate and the film stack did not improve the mean-square-error (MSE) values of the SE model and was not included in the fits.

Figure 3 shows the film thickness and void fraction of processed films as determined by spectroscopic ellipsometry. The film thickness remained approximately constant, within the scatter in the data, as a function of number of cycles and exposure time to the ICP (Fig. 3, upper panel). Conversely, the void fraction tends to increase with increasing number of cycles, with the 120 cycles ($t_2/t_1 = 6/4$), 480 cycles, and continuous rotation samples containing the three highest % voids (Fig. 3, lower panel). This result is consistent with mass spectrometric analysis of the reaction products upon exposure of a film to the ICP following deposition in the CCP (see Sec. III F). Product evolution occurred by hydrogen etching throughout the film thickness, resulting in

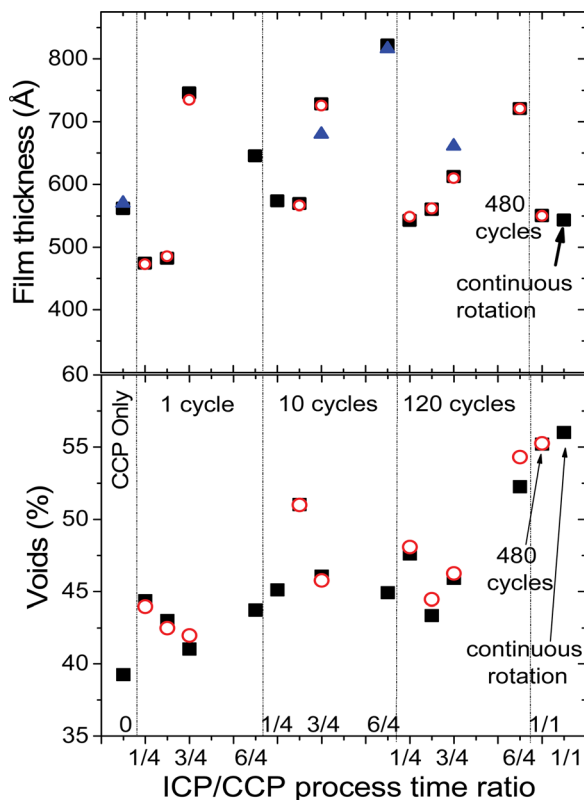


Fig. 3. (Color online) Film thickness and % voids determined by spectroscopic ellipsometry for different ICP/CCP process time ratios. Data are grouped according to the number of process cycles. Open circles indicate duplicate experiments of most solid squares, an indication of reproducibility. Films deposited with a large number of process cycles (480 cycles and continuous cycling) had ICP/CCP process time ratio of 1.

increasing void fraction with ICP exposure time. As the number of cycles increased, the layer thickness per cycle decreased. Since it was easier for H-atoms to diffuse through a thinner layer, the result was higher etching rate and more porosity.

B. Raman spectroscopy

Raman spectra of each sample were deconvoluted into three Gaussian features (Fig. 4) with peaks at 480 ($480 \pm 2 \text{ cm}^{-1}$) attributed to the amorphous component, at 520 cm^{-1} ($519 \pm 1.6 \text{ cm}^{-1}$) attributed to the crystalline component (c-Si), and near 510 cm^{-1} (502 cm^{-1} to 512 cm^{-1} , or $507 \pm 3 \text{ cm}^{-1}$) attributed to nanocrystallites (nc-Si).^{30–33} Attempts were made to fit spectra to two Gaussians, but the χ^2 values were larger than a three-component fit when the 520 cm^{-1} peak was discernible. Based on the three-peak analysis, films contained from 100% to 30% amorphous material, for the range of conditions investigated.

Figure 5 shows Raman spectra of samples subjected to various deposition/nanocrystallization conditions. Each panel corresponds to the same number of cycles (n_c) and the same deposition time (t_1), but variable crystallization time (t_2). For all experiments in Fig. 5, the *total* deposition time ($n_c \times t_1$) was kept constant at 40 min. Thus, as the number of cycles increased, the CCP exposure time and the resulting film thickness deposited per cycle decreased. Figure 5(a) shows the spectra for 1 cycle with $t_1 = 40$ min deposition in the CCP, followed by exposure to the H_2 ICP for times t_2 of 0, 10, 20, 30, and 60 min. The spectra indicate that the films contain mostly amorphous Si, except when the H_2 ICP exposure time was 60 min ($t_1/t_2 = 40/60$ min), for which a small peak at 520 cm^{-1} indicates the conversion of a small fraction of material to crystalline Si. When the number of cycles was increased to 10, and the deposition time per cycle was correspondingly reduced to 4 min, formation of Raman-active crystallites was just discernible at $t_1/t_2 = 4 \text{ min}/3 \text{ min}$ [Fig. 5(b)]. With 120 cycles and a very short deposition time per cycle of 20 s, crystallites formed at $t_1/t_2 = 20 \text{ s}/5 \text{ s}$ [Fig. 5(c)].

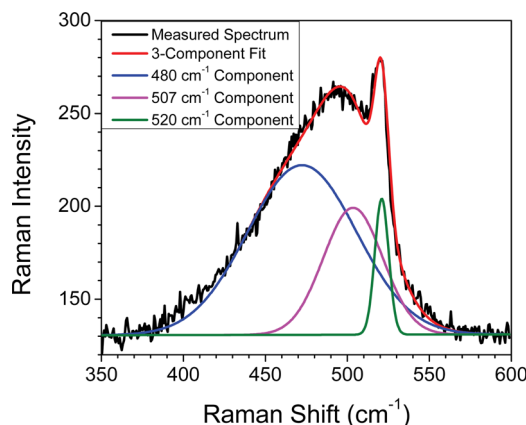


Fig. 4. (Color online) Example of a three Gaussian-peak fit to Raman data of a sample analyzed to contain 62% a-Si, 31% nc-Si, and 7% c-Si based on the integrated area of the 480 cm^{-1} , 507 cm^{-1} , and 520 cm^{-1} Raman peaks, respectively. Process conditions correspond to 120 cycles with an ICP/CCP time ratio of 1.5.

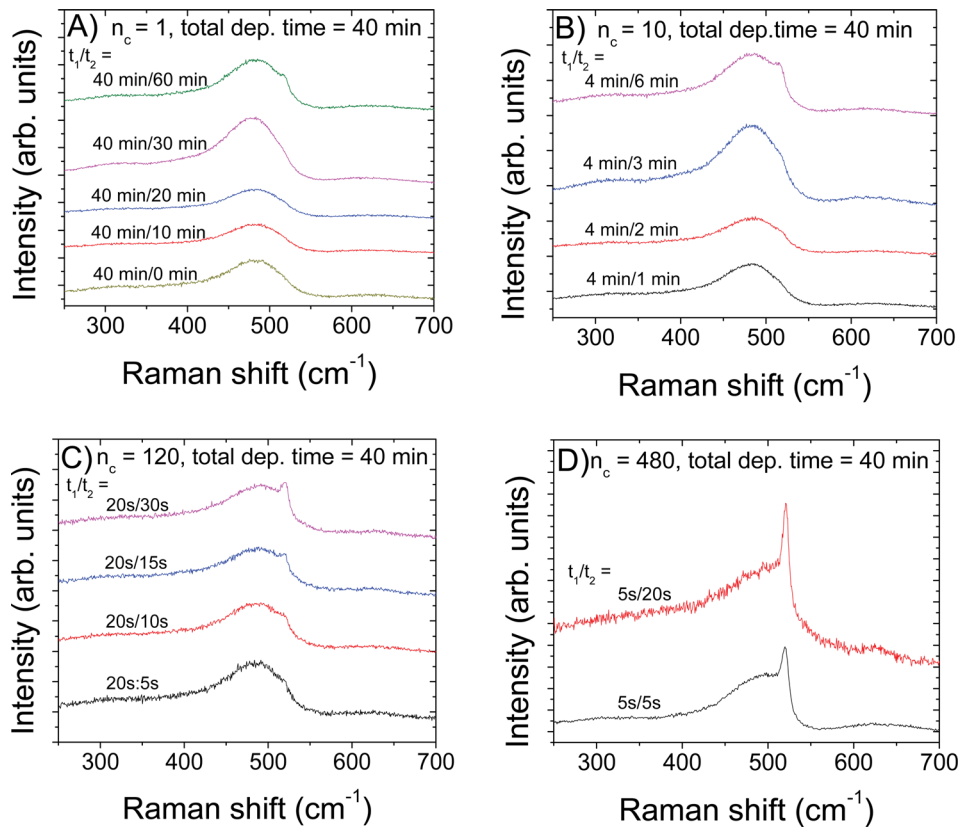


Fig. 5. (Color online) Raman spectra of films deposited at a substrate temperature of 250 °C with the same *total* deposition time ($n_c \times t_1$) of 40 min, and variable ratio of deposition time to nanocrystallization time t_1/t_2 , resulting by varying the number of cycles, n_c : (a) $n_c = 1$, (b) $n_c = 10$, (c) $n_c = 120$, and (d) $n_c = 480$.

Finally, a deposition time of 5 s per cycle [Fig. 5(d)], 480 cycles at $t_1/t_2 = 5\text{ s}/20\text{ s}$ (upper curve) or 480 cycles at $t_1/t_2 = 5\text{ s}/5\text{ s}$ (lower curve), resulted in prominent crystalline peaks near 520 cm^{-1} . Based on these results, it was concluded that the thinner the a-Si:H layer deposited in the CCP per cycle, the less exposure time in the hydrogen ICP was needed to induce crystallization.

The total crystalline volume fraction (larger crystallites plus nanocrystallites), X_c , was estimated from the deconvoluted spectra using^{30,31}

$$X_c = \frac{I_{510} + I_{520}}{yI_{480} + I_{510} + I_{520}}, \quad (1)$$

where I_{480} , I_{510} , and I_{520} are the integrated areas of the three individual Gaussian peaks at 480 cm^{-1} , 510 cm^{-1} , and 520 cm^{-1} , respectively, and y is the ratio of Raman cross-sections for crystal-to-amorphous silicon (σ_c/σ_a).^{34–36} A value of $y = 1$ was used.³⁰ The volume fraction of larger crystallites was obtained by using just the intensity of the 520 cm^{-1} peak in the numerator of Eq. (1).

Figure 6 shows a plot of the crystalline volume fraction X_c from Eq. (1) for just the larger crystallites [Fig. 6(a)] and for both larger and nanocrystallites [Fig. 6(b)]. For a given number of cycles and total deposition time, the crystalline volume fraction X_c increased as the ratio t_2/t_1 increased. The number of cycles determines the thickness of the deposited

film per cycle. Since the total deposition time was kept constant, more cycles means a thinner film per cycle. A thinner film can be crystallized more readily than a thicker film, since H atoms need to diffuse a shorter distance from the surface to the bottom of the film. Thus, for a given film thickness after deposition, the longer the exposure to the ICP the higher the crystalline content of the film.

The average deposition rate measured by spectroscopic ellipsometry was $15.6 \pm 2.7\text{ \AA}/\text{min}$. Therefore, for a 40 min total deposition time, the thickness of the layer deposited per cycle was 624, 62, and 5.2 \AA for 1, 10, and 120 cycles, respectively. For a 10-cycle film, a 6 min H_2 ICP exposure per cycle resulted in 20% crystalline Si (Fig. 6). When monolayer and submonolayer amounts of material were deposited per cycle (480 cycles, $t_1 = 5\text{ s}$ per cycle, $\sim 1.3\text{ \AA}/\text{cycle}$ and 4500 cycles, $t_1 = 1.6\text{ s}$, $\sim 0.45\text{ \AA}/\text{cycle}$), with equal H_2 ICP exposures ($t_2/t_1 = 1$), $\sim 50\%$ crystalline material was obtained in both cases (also shown in Fig. 6). The degree of crystallinity for $n_c = 120$ at $t_2/t_1 = 1$ was $\sim 25\%$ (interpolated). These data indicate that a “saturation” effect in the degree of crystallization was obtained as the number of cycles was increased, and the amount of material deposited per cycle approached one monolayer. Such saturation is expected, since one monolayer or less of material deposited per cycle is equivalent to the case of a sample continuously exposed to both SiH_x from the silane CCP and H atoms from the H_2 ICP.

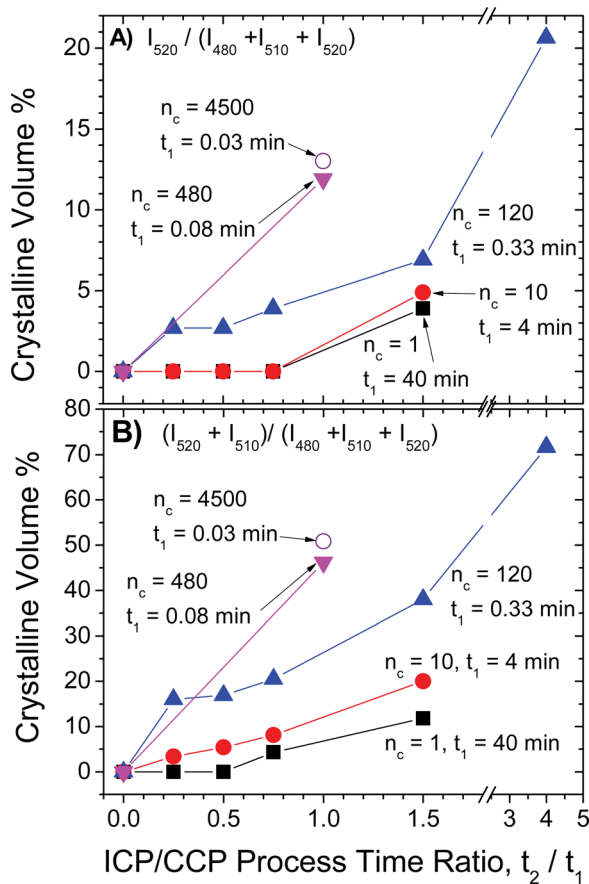


Fig. 6. (Color online) Crystalline volume fraction as a function of ICP to CCP exposure time ratio, using (a) just the c-Si peak at 520 cm^{-1} , or (b) both the c-Si peak and the 510 cm^{-1} nc-Si peak. CCP deposition times t_1 (0.08 min, 0.3 min, 4 min, and 40 min), correspond to number of cycles n_c (480, 120, 10, and 1), respectively. The total CCP exposure time ($n_c \times t_1$) is the same (40 min) for all samples. Crystalline volume fraction was estimated using Raman spectra fit with three Gaussian-peaks.

Multivariate statistical modeling of the crystalline Si content of the films measured by Raman scattering was carried out using two experimental variables: the number of process cycles (n_c) and the ICP/CCP time ratio (t_2/t_1). The 510 cm^{-1} and 520 cm^{-1} features did exhibit a high degree of correlation (correlation coefficient >0.95). However, about one fourth of films exhibiting the 510 cm^{-1} nc-Si feature did not display a 520 cm^{-1} c-Si feature [compare in Figs. 6(a) and 6(b) the $n_c = 10$ points for $t_2/t_1 = 0.25, 0.5$ and 0.75 and the $n_c = 1, t_2/t_1 = 0.75$ point]. This supports a mechanism in which the nc-Si material responsible for the 510 cm^{-1} band is a precursor to larger crystallites that have a well-developed band-structure and the Raman characteristics identifiable with bulk crystalline silicon. The model using both process variables and the two Raman crystalline materials was able to explain over 90% of the variation in all the experimental data with a 95% confidence level.

Figure 6 shows a threshold behavior at low number of cycles [e.g., 1 cycle in Fig. 6(b)], suggesting that the number of cycles is very important during the nucleation phase of crystallization. Once nucleation occurs, longer exposure times to H-atoms results in grain growth. Thus, once a

substantial (experimentally controlled) amount of material giving rise to the 510 cm^{-1} Raman feature is nucleated, larger grains can be grown by increasing the ICP/CCP process time ratio. Also, the fraction of 520 cm^{-1} material never exceeded the fraction of 510 cm^{-1} material, supporting the belief that the material responsible for the 510 cm^{-1} Raman peak was a prerequisite to the formation of larger crystallites that contributed to the 520 cm^{-1} feature.

Raman spectra were also used to estimate the size of crystallites. Methods proposed in the literature include: (a) the shift of the nominal 520 cm^{-1} peak,^{37,38} (b) the shift of the band in the $504\text{--}512\text{ cm}^{-1}$ region,³⁹ and (c) the shift in the 510 cm^{-1} peak throughout the $480\text{--}520\text{ cm}^{-1}$ range.^{40,41} These correlations of peak position are restricted to crystallite sizes $<150\text{--}200\text{ \AA}$. Figure 7 shows a comparison of the three methods for estimating the crystallite size in the films. Disparities between the methods are seen at small crystallite sizes and also at large crystallite sizes. The peak-position formalism of method (a)^{40,41} (black squares in Fig. 7) was adopted in the present work

$$L(\text{\AA}) = \sqrt{\frac{8843}{\omega_0 - \omega_L}}, \quad (2)$$

where L is the crystal size associated with the maximum in the transverse-optical (TO) Raman feature (ω_L) and ω_0 is assumed to have the single crystal value of 520 cm^{-1} . Figure 7 shows that these data [obtained using Eq. (2)] lie between the other two sets of measurements in the range of ~ 510 and 518 cm^{-1} .

Using Eq. (2) and the Raman positions obtained by the three-peak fitting, the histogram of crystallite sizes in Fig. 8 was generated. The symbols identify three films, and the processing conditions, which exhibited only a 480 cm^{-1} Raman feature (@), both a 480 cm^{-1} and a 510 cm^{-1} Raman feature (#), and all three ($480, 510, \text{ and } 520\text{ cm}^{-1}$) Raman

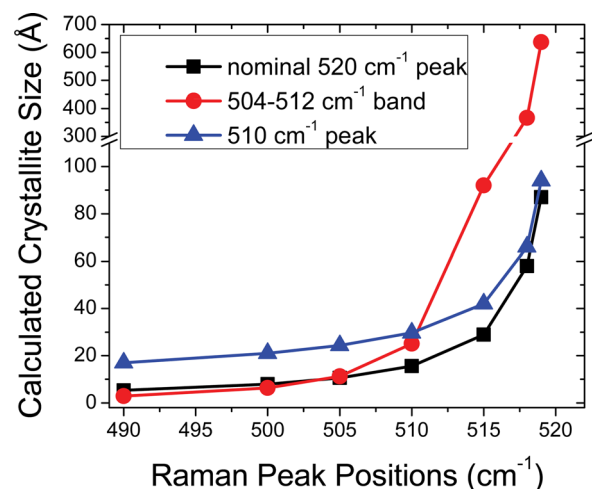


Fig. 7. (Color online) Comparison of three literature methods using the shift in Raman peak positions to estimate crystallite size, based on: position of the nominal 520 cm^{-1} peak (black squares), position of the band in the $504\text{--}512\text{ cm}^{-1}$ region (red circles), and position of the 510 cm^{-1} peak (blue triangles).

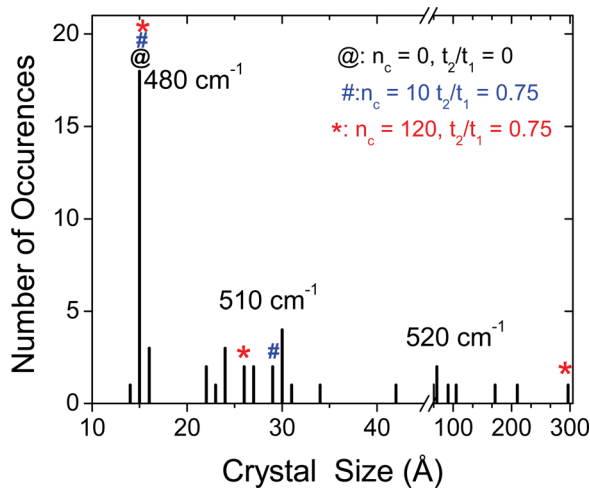


Fig. 8. (Color online) Histogram of crystallite sizes associated with the peaks in the 480, 510, and 520 cm^{-1} regions of the Raman fits. The three groupings indicate the Raman feature analyzed for determining crystallite size. Stars highlight crystal sizes and processing conditions for three samples for which TEM analysis was available (see Fig. 10). The spectrum for $n_c = 0$, $t_2/t_1 = 0$ (@) exhibited only a 480 cm^{-1} feature; the spectrum for $n_c = 10$, $t_2/t_1 = 0.75$ (#) exhibited a 480 cm^{-1} and a 510 cm^{-1} features, and the spectrum for $n_c = 120$, $t_2/t_1 = 0.75$ (*) exhibited all three (480, 510, and 520 cm^{-1}) Raman features.

features (*). These three films were also used for TEM measurements. Figure 8 shows that the crystallite size distribution breaks into three groups identified by the Raman peaks labeled in the figure. These data represent 66 measurements and 17 different process conditions; yet, there are distinctive gaps in the size distribution between the 15 Å group, the 25–30 Å group, and the 70+ Å group. It should be noted that each of the three Raman peaks referred to above likely represents a superposition of Raman peaks contributed by varying size particles, each having smaller Gaussian-widths. However, the final result is not a single broad distribution, but three distinct populations. Slaoui *et al.*⁴² formed Si-rich

nanoparticles by electron cyclotron resonance PECVD, which on annealing yielded discrete size ranges in energy-filtered TEM images centered at ~ 15 , ~ 30 , ~ 40 , and ~ 55 Å. The results of the present work seem to parallel their findings.

C. Transmission electron microscopy

Figure 9 shows cross sectional dark-field TEM images of samples with different t_1 and t_1/t_2 . The extent of the film is indicated in each of the three panels by a two-way vertical arrow. The Au-Pd layer shown on top of each film was employed to avoid charging during sample preparation using FIB. Selected crystallites are enclosed in red rectangles.

Without H_2 plasma exposure [Fig. 9(a)], a few small nanocrystallites could be identified at the interface between the film and the glass substrate. These crystallites could have nucleated on contaminants on the surface of the glass substrate. The TEM of the film that was subjected to ten cycles of CCP deposition and H_2 ICP crystallization ($X_c = 24\%$), showed a columnar structure of crystallites along the growth direction [Fig. 9(b)]. This finding suggests that nanocrystallization did not occur only on the surface or near surface region of the film after each layer was deposited and then exposed to the H_2 ICP, but throughout a substantial volume of the film. In the selective etching model of nanocrystallization, the etching rate of the amorphous phase was about 10–20 times faster than that of the crystalline phase,^{43,44} and etching took place on the surface of the film.⁴³ If this surface etching mechanism were operative, a layered distribution of crystallites parallel to the surface of the film should be observed. Instead, the growth of columnar crystallites preferentially perpendicular to the film surface in the present study suggests that selective etching is not the primary mechanism for nanocrystallization, at least under the conditions employed.

The sample subjected to 5 s deposition in the CCP and then 20 s exposure to the ICP per cycle (for a total of 120 cycles) contains a larger amount of nanocrystallites [Fig. 9(c)]. The

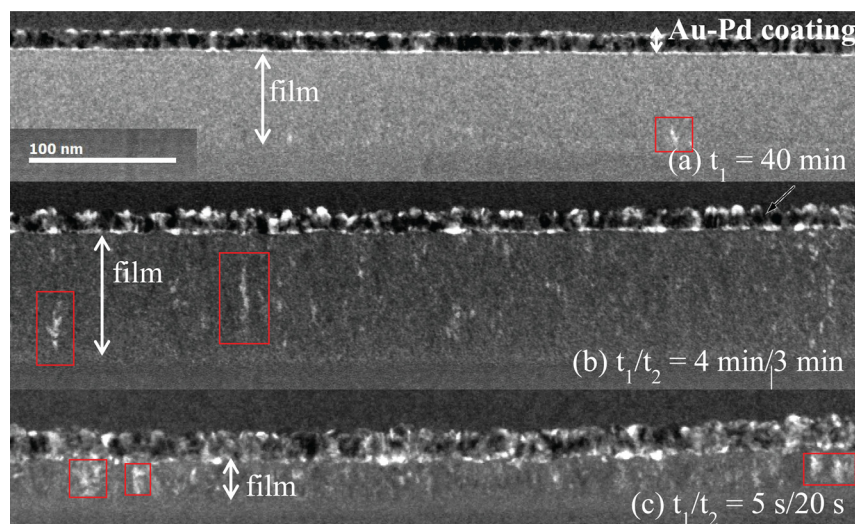


Fig. 9. (Color online) Cross sectional dark-field TEM images of samples with different t_1 and t_1/t_2 . Selected crystallites are enclosed in red rectangles. (a) $t_1 = 40$ min, $t_2 = 0$, total deposition time = 40 min, (b) $t_1 = 4$ min, $t_2 = 3$ min, total deposition time = 40 min, (c) $t_1 = 5$ s, $t_2 = 20$ s, total deposition time = 10 min. The extent of the film thickness is indicated in each of the three panels by a two-way vertical arrow. The Au-Pd layer shown on top of each film was employed to avoid charging during sample preparation using FIB.

thickness of that sample deduced from the TEM image was around 200–250 Å. Some columnar crystallites traversed the entire thickness of the film. The columns were wider than those of the sample in Fig. 9(b). The crystalline volume fractions estimated by counting crystallites in the dark-field TEM were in qualitative agreement with the Raman results in Fig. 6, considering the uncertainty in the TEM counting method.

To further assess the Raman results, bright field high-resolution TEM analysis was performed on several samples. Figure 10 shows the HRTEM images of samples with: (a) only a-Si:H deposition, no ICP exposure; (b) a 10 cycle process ($t_2/t_1 = 3 \text{ min}/4 \text{ min}$); and (c) a 120 cycle process ($t_2/t_1 = 15 \text{ s}/20 \text{ s}$). Each micrograph represents approximately the upper half of each of the films and the identified (at least three lattice fringes separated by $\sim 3\text{Å}$) grains are outlined in red. Without additional H_2 plasma exposure (the CCP deposition gas contained 40% H_2), small crystallites were observed (panel A) even though this process condition resulted in only a 480 cm^{-1} feature in the Raman spectrum that is normally assigned exclusively to amorphous material. In any case, Fig. 10 suggests that nucleation occurred randomly in the bulk, and that crystallite size increased with H_2 plasma exposure and the number of process cycles, consistent with the results of Figs. 5 and 6. It also appears that

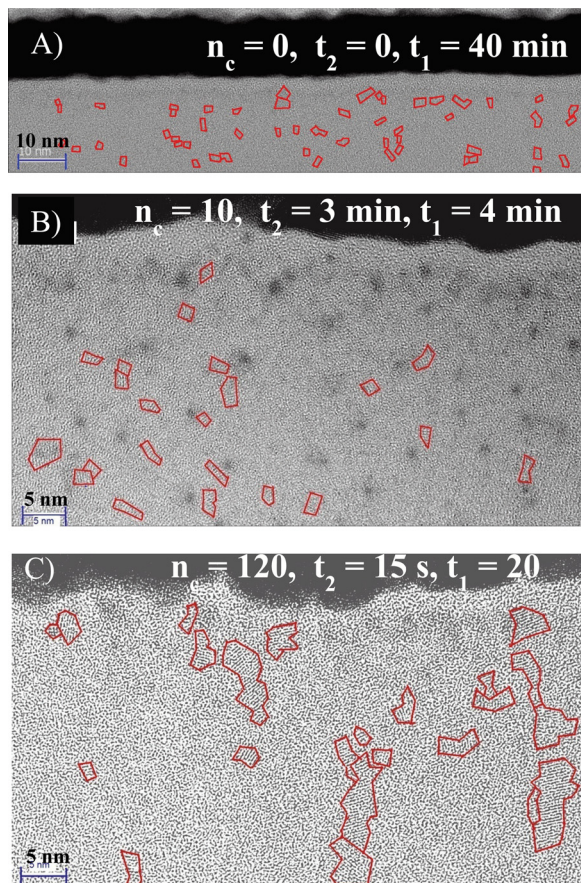


Fig. 10. (Color online) High resolution TEM of three samples exhibited (a) only the 480 cm^{-1} Raman feature, (b) both the 480 and 510 cm^{-1} Raman features, and (c) all three (480 , 510 , and 520 cm^{-1}) Raman features. Grains are outlined. Scale marker indicates 10 nm or 5 nm.

grains show some preference to grow or coalesce in the direction normal to the surface (the growth direction).

Figure 11 shows histograms of the crystallite sizes counted using the HRTEMs of the three films of Fig. 10. These three films (exhibiting only a 480 cm^{-1} feature, both the 480 cm^{-1} and 510 cm^{-1} features, and all three Raman features) correspond to the histogram bins marked by the symbols in Fig. 8. There is a significant similarity between the crystallite size distribution exhibited by the three films examined by TEM, and the distribution observed for all films based on the Raman estimates (Fig. 8). The distributions based on the TEMs are broader than those obtained by Raman; yet, the most prevalent sizes persist in both distributions.

D. Fourier transform infrared spectroscopy

Transmission FTIR spectroscopy was used to characterize a few of the films deposited on Si substrates. A film deposited in the CCP for 40 min and then exposed to the D_2 plasma had a strong SiH stretch near $2000\text{--}2100 \text{ cm}^{-1}$ and little if any SiD stretch at $1500\text{--}1600 \text{ cm}^{-1}$. Conversely, a

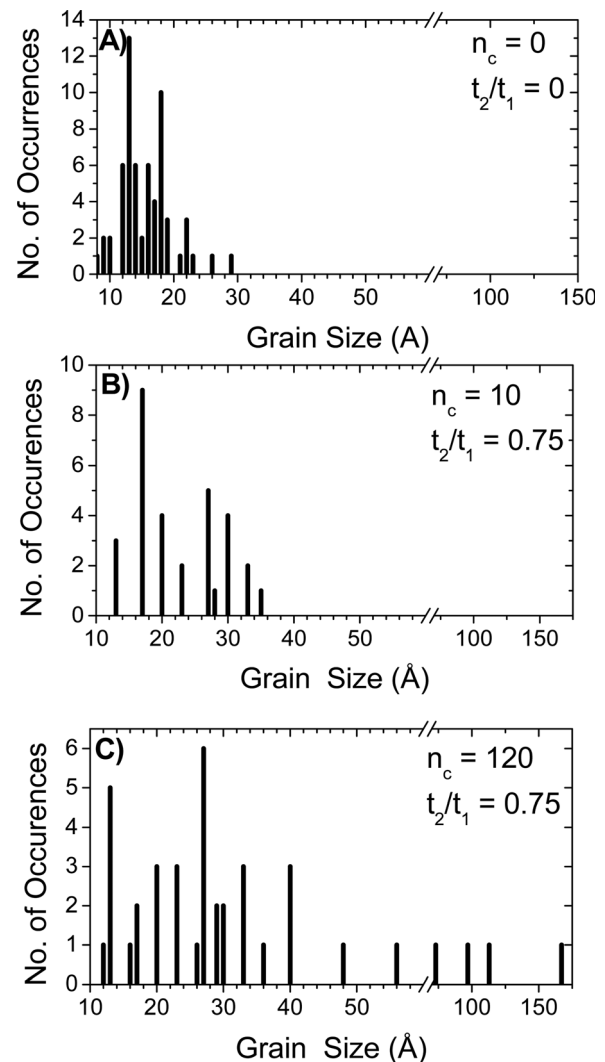


Fig. 11. Histograms of the grain-size distributions obtained from the TEM micrographs of Fig. 10. The precision of the grain-size axis is $\sim \pm 2 \text{ Å}$ in A) and $\sim \pm 1 \text{ Å}$ in B) and C).

sample subjected to ten cycles, each of 4 min CCP deposition and 6 min of D₂ ICP treatment, exhibited a clear SiD stretch, and no SiH stretch. Agarwal *et al.*⁴⁶ used surface-sensitive total internal reflection FTIR and found a similar displacement of H when a-Si:H was exposed to D atoms in a deuterium plasma, albeit more representative of the surface of the film. Since the entire film was analyzed by the transmission FTIR measurements in the present study, surface reactions are virtually invisible and the measurements indicate that D displaces all of the H in the bulk of the film.

E. Mass spectrometry

To help understand the transition from amorphous to nanocrystalline silicon, experiments were conducted using D₂ instead of H₂ in the ICP to distinguish H in the starting film from H incorporated in the film during ICP exposure. Deuterated silicon etching products formed in the ICP were detected with a mass spectrometer. Unfortunately, the signal of HD (atomic mass unit, AMU 3) could not be separated from the large background from D₂ (AMU 4) and D and H₂ (AMU 2). Ions formed in the ionizer by electron impact of the etching products SiH_xD_{4-x} ($x = 0, 1, 2, 3, 4$) at AMU 29 (SiH⁺), 30 (SiH₂⁺, SiD⁺), 31 (SiH₃⁺, SiHD⁺), 32 (SiH₂D⁺, SiD₂⁺), 33 (SiHD₂⁺), and 34 (SiD₃⁺) were observed during the D₂ ICP exposure.

Figure 12 shows the time evolution of the major signal at AMU 34 (SiD₃⁺, assumed to originate mainly from SiD₄) when a sample with an a-Si:H film grown in the CCP is exposed at time $t = 0$ to a D₂ ICP. The starting film thickness was varied as: (a) 168 Å, (b) 112 Å, (c) 84 Å, (d) 56 Å, and (e) 28 Å, corresponding to deposition times of 12, 8, 4, 2, 1, and 1/3 min, respectively. Note that the 84 Å and 56 Å films correspond to approximately the deposition-per-cycle thickness observed in the range of ten-cycle data described earlier. As the starting film thickness increases, it takes longer for the signal to drop to the baseline. However, even after the signal decayed to the baseline, the film thickness, measured by UV-VIS absorption, hardly changed. This suggests

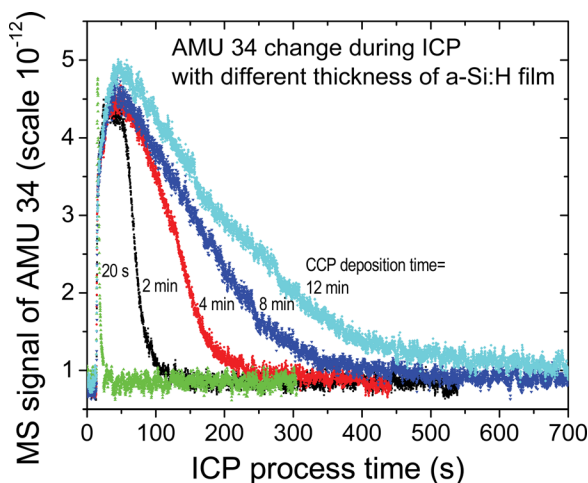


FIG. 12. (Color online) Mass spectroscopic signal (AMU 34) as a function of D₂ ICP exposure time for films grown in the CCP for different deposition times (and therefore different thicknesses) ranging from 20 s to 12 min.

that etching occurred in the volume of the film, increasing the film porosity. If etching occurred only at the surface the signal should have either (1) quickly reached a plateau (independent of film thickness) and then decayed to baseline as the film cleared, or (2) decayed rapidly to zero, or nearly so (again independent of film thickness), as a rapidly etched surface layer was removed and little or no etching of the bulk film occurred. Neither of these scenarios is consistent with the measurements in Fig. 12.

The flow rate of reaction product (SiD₄) emanating from the film can be estimated from the intensity of the daughter ion (SiD₃⁺) signal after calibration. First, a flow of SiH₄ gas (1% in He) was established in the ICP chamber and the signal ($S_{\text{SiH}_3^+}$) of SiH₃⁺ (AMU 31) was recorded. The feed gas was switched to D₂ and power to the ICP was turned on. The signal $S_{\text{SiD}_3^+}$ was recorded, corresponding to SiD₄ product in the D₂ ICP. Assuming that SiH₃⁺ and SiD₃⁺ were formed in the MS ionizer through dissociative ionization reactions



the partial pressure of SiD₄ can be determined from the relationship

$$\frac{S_{\text{SiD}_3^+}}{S_{\text{SiH}_3^+}} = \frac{P_{\text{SiD}_4}}{P_{\text{SiH}_4}} \cdot \frac{\sigma_{\text{SiD}_4}}{\sigma_{\text{SiH}_4}}, \quad (5)$$

where P_{SiH_4} is the SiH₄ partial pressure, P_{SiD_4} is the partial pressure of the etch product SiD₄, and $\sigma_{\text{SiD}_4}/\sigma_{\text{SiH}_4}$ is the ratio of dissociative ionization cross sections of SiD₄ and SiH₄ to form SiD₃⁺ and SiH₃⁺, respectively. ($\sigma_{\text{SiD}_4}/\sigma_{\text{SiH}_4} = 1.062$ at 70 eV).⁴⁵ The SiD₄ partial pressure in the D₂ ICP can then be obtained from Eq. (5), knowing P_{SiH_4} and the measured signal intensities.

The SiD₄ flow rate was then be computed from the partial pressures

$$\frac{P_{\text{SiD}_4}}{P_{\text{D}_2}} = \frac{f_{\text{SiD}_4}}{f_{\text{D}_2}}, \quad (6)$$

where f_{SiH_4} is the known flow rate of SiH₄ used at the start. Assuming $P_{\text{SiD}_4} \ll P_{\text{D}_2}$, then P_{D_2} is the known ICP chamber pressure, and f_{SiD_4} can be found from Eq. (6). Thus, an etching rate of 2.5 ± 0.3 Å/min can be computed for the film in the D₂ plasma, independent of film thickness. Consequently, about 18% of the mass of the film is removed in the D₂ plasma. The mass spectrometry measurements of the evolution of SiD₄ as a function of time are also compared with the results of a mathematical model describe below.

F. Mathematical model

The results presented above suggest that H (or D) diffuses through the film and induces crystallization by a mechanism that generates SiH₄ (or SiH_xD_{4-x}) in parallel and perhaps as a byproduct to H abstraction or “chemical annealing”¹⁶ by diffusing H (or D). A simple mathematical model of etching

product formation and diffusion upon exposure of an a-Si:H film to a D₂ plasma was developed to explain the behavior depicted in Fig. 12. The main assumptions of the model were: (1) D atoms formed in the plasma diffuse into the film, and react with silicon moieties to produce volatile SiD₄, which diffuses out, (2) reaction of D atoms is first order in D atom concentration and occurs throughout the film volume, (3) as D reacts with silicon in the film to yield volatile product, the void fraction of the film increases, but the film thickness remains unchanged, (4) the D concentration at the film surface exposed to the plasma is maintained constant by D₂ dissociation, and (5) the concentration of SiD₄ at the film surface is kept zero as gas flow sweeps the reaction product away. The mathematical model consisted of the 1-D (as a function of depth in the film) time-dependent mass balance equations for D atoms and SiD₄.

The diffusion coefficients of D and SiD₄ in the film, as well as the rate coefficient of the etching reaction, were treated as fitting parameters. The results in Fig. 12 could

only be reproduced if the diffusion coefficients increased over time. The diffusion coefficients of D-atoms and etching product SiD₄ in the bulk of the film were assumed to have the form

$$D_D = (0.61618 - 0.01652 t + 1.3376 \times 10^{-4} t^2) \times 10^{-19} \text{m}^2/\text{s}, \quad (7)$$

$$D_{\text{SiD}_4} = (0.01356 + 0.00325 t) \times 10^{-19} \text{m}^2/\text{s}, \quad (8)$$

where time t is in s.

According to Eq. (7), the diffusion coefficient of D atoms increases from $6.6 \times 10^{-20} \text{m}^2/\text{s}$ to $4.4 \times 10^{-19} \text{m}^2/\text{s}$ after 4 min of D₂ plasma exposure. Magee and co-workers^{47,48} reported diffusion coefficients for D in a-Si:H in the range of $3 \times 10^{-21} \text{m}^2/\text{s}$ to $6.95 \times 10^{-19} \text{m}^2/\text{s}$ at 250 °C, so the values found in the present study are reasonable. From Eq. (8), the diffusion coefficient of SiD₄ increases from $1.4 \times 10^{-21} \text{m}^2/\text{s}$ to $7.9 \times 10^{-20} \text{m}^2/\text{s}$ after 4 min exposure to the

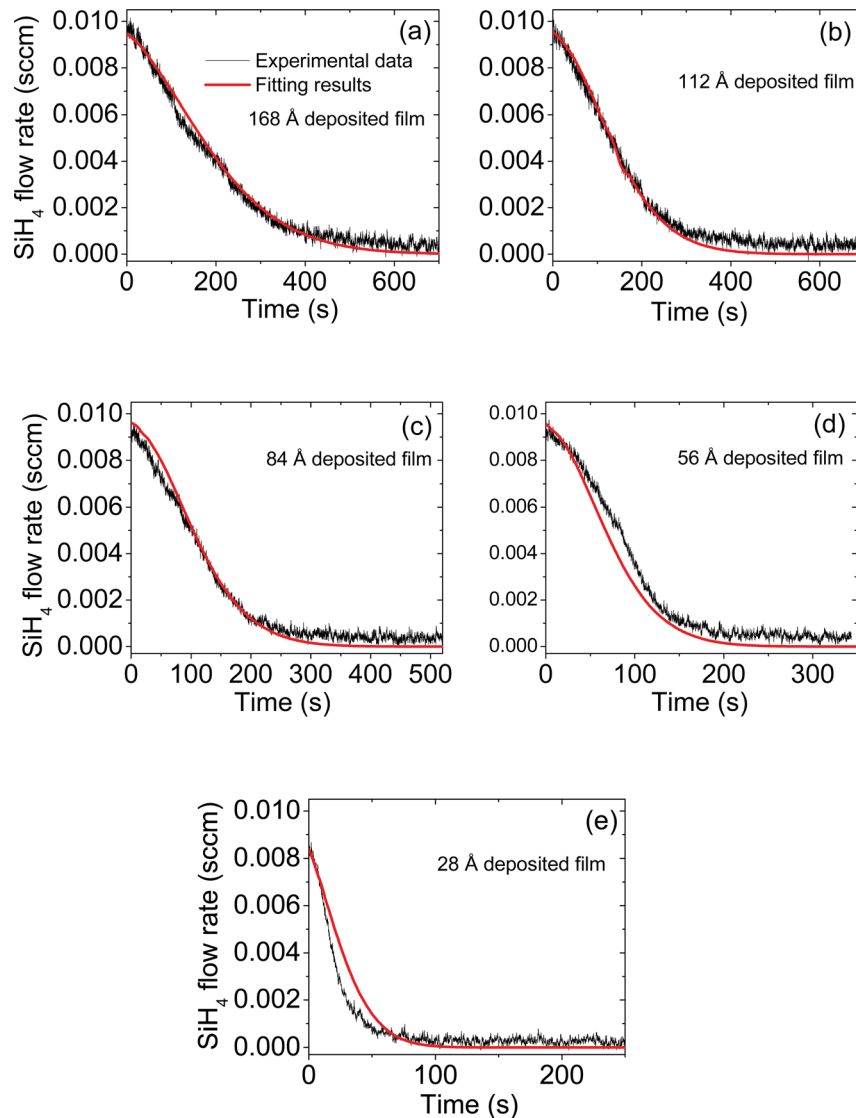


FIG. 13. (Color online) Comparison between measured and predicted flow rate of SiD₄ emanating when an a-Si:H film deposited in the CCP is exposed to a D₂ ICP starting at time $t = 0$. Starting film thickness was: (a) 168 Å, (b) 112 Å, (c) 84 Å, (d) 56 Å, and (e) 28 Å.

plasma. These increases in D and SiD₄ diffusivity are attributed to an increasing void fraction in the film as a result of etching (see Fig. 3). Voids that form in the first 4 min of exposure to the D₂ plasma speed up diffusion of the much larger, chemically inert SiD₄ (~59-fold), compared to D (~7-fold). Diffusivity values for SiD₄ (or SiH₄) in a-SiH could not be found in the published literature.

Figure 13 shows a comparison between measured and predicted time evolution of the flow rate of SiD₄ when an a-Si:H film deposited in the CCP was exposed to a D₂ plasma starting at time $t=0$. Different panels correspond to different starting film thickness (proportional to exposure time in the CCP). The decay of the product flow emanating from the film is predicted fairly well for all five cases.

IV. SUMMARY AND CONCLUSIONS

Layer-by-layer (LbL) growth and nanocrystallization of a-Si:H thin films was investigated using a dual-plasma source reactor to spatially separate film deposition and subsequent nanocrystallization. Heated substrates were mounted on a susceptor that was rotated sequentially into a CCP fed with SiH₄/He/H₂ gas to deposit an a-Si:H layer, followed by exposure to a H₂ ICP to induce crystallization in the layer. Under computer control, deposition and crystallization times could be varied from 40 min/cycle to <2 s/cycle. Adjusting the time spent in the silane CCP and hydrogen ICP allowed exploration of the effects of each plasma over a wide range from no exposure to the ICP, to an ICP/CCP exposure duration ratio of 4/1. Postprocess SE, Raman spectroscopy, FTIR, and TEM, as well as mass spectrometry provided valuable insights into cyclic processing.

For a nearly constant total thickness, films grown with many shorter cycles of silane CCP deposition followed by H₂ ICP crystallization exhibited a higher percentage of crystalline material than those films grown with fewer longer cycles. Also, for a given silane CCP exposure time, the percent crystalline material increased with increasing time in the H₂ ICP. Significantly, H₂ ICP-induced nanocrystallization resulted in continuous distributions of crystalline Si grains as a function of depth, and not in layered grains with a periodicity corresponding to the number of cycles used, indicating that crystallization occurred throughout the volume of the films.

The region of layer-by-layer parameter space studied allowed some control of grain size of deposited films. For example, films with grain sizes of 10–20 Å were prepared under baseline a-Si:H deposition conditions, while films containing two crystal size ranges (10–20 Å and 20–30 Å) were prepared by a ten-cycle process with short H-atom exposure times ($t_2/t_1 = 3/4$ min). The fact that almost all of the crystallite grain sizes estimated by TEM and Raman fell into distinct size groups suggested some mechanism for limited growth of certain crystallite sizes.

Crystallization was accompanied by evolution of SiD₄ (when using a D₂ instead of H₂ plasma), detected by mass spectrometry. A mathematical model revealed a diffusion-controlled etching process with the diffusion coefficients increasing over time,

especially for SiD₄. This enhancement in diffusivities was attributed to increasing void fraction in the films with prolonged exposure to the H₂ ICP. The presence of voids in the films was also suggested by SE measurements.

The dual-plasma reactor with rotating substrates studied in this work could also benefit other layer-by-layer processes, such as atomic layer deposition (ALD) and atomic layer etching (ALET). Both of these processes are crucial as device critical dimensions approach monolayer thickness.

ACKNOWLEDGMENTS

The authors are grateful to the University of Houston GEAR program, and the Department of Energy, Office of Fusion Energy Science, contract DE-SC0001939 for financial support of this work. Raman measurements by Milko Iliev of the Texas Center for Superconductivity, University of Houston, and TEM measurements by LAM Research Corp. are also gratefully acknowledged.

- ¹L. L. Kazmerski, *J. Electron Spectrosc. Relat. Phenom.* **150**, 105 (2006).
- ²M. Z. Jacobson, *Energy Environ. Sci.* **2**, 148 (2009).
- ³M. A. Green, *Prog. Photovolt.: Res. Appl.* **17**, 183 (2009).
- ⁴X. Deng and E. A. Schiff, "Amorphous silicon-based solar cells," in: *Handbook of Photovoltaic Science and Engineering*, edited by A. Luque and S. S. Hegedus, (Wiley, West Sussex, 2003), p. 505.
- ⁵M. Vanecek, A. Poruba, Z. Remes, N. Beck, and M. Nesladek, *J. Non-Cryst. Solids* **227–230**, 967 (1998).
- ⁶R. E. I. Schropp and M. Zeman, *Amorphous and Microcrystalline Silicon Solar Cell: Modeling, Materials and Device Technology* (Kluwer Academic, Norwell, 1998).
- ⁷H. M. Branz, *Phys. Rev. B* **60**, 7725 (1999).
- ⁸F. Meillauda *et al.*, *Philos. Mag.* **89**, 2599 (2009).
- ⁹M. Vanecek, A. Poruba, Z. Remes, J. Rosa, S. Kamba, V. Vorlicek, J. Meier, and A. Shah, *J. Non-Cryst. Solids* **266–269**, 519 (2000).
- ¹⁰J. R. Abelson, *Appl. Phys. A* **56**, 493 (1993).
- ¹¹A. Matsuda, *J. Non-Cryst. Solids* **59–60**, 767 (1983).
- ¹²D. C. Marra, E. A. Edelberg, R. L. Naone, and E. S. Aydil, *J. Vac. Sci. Technol. A* **16**, 3199 (1998).
- ¹³S. Sriraman, M. S. Valipa, E. S. Aydil, and D. Maroudas, *J. Appl. Phys.* **100**, 053514 (2006).
- ¹⁴G. N. Parsons, *Appl. Phys. Lett.* **59**, 2546 (1991); E. Srinivasan and G. N. Parsons, *ibid.* **72**, 456 (1998).
- ¹⁵M. Fang, J. B. Chévrier, and B. Drévillon, *J. Non-Cryst. Solids* **137–138**, 791 (1991).
- ¹⁶H. Shirai, B. Drévillon, and I. Shimizu, *Jpn. J. Appl. Phys.* **33**, 5590 (1994).
- ¹⁷A. Asano, *Appl. Phys. Lett.* **56**, 533 (1990). For the reactor configuration see A. Asano, T. Ichimura, and H. Sakai, *J. Appl. Phys.* **65**, 2439 (1989).
- ¹⁸P. Roca i Cabarrocas, J. B. Chévrier, J. Huc, A. Lloret, J. Y. Parey, and J. P. M. Schmitt, *J. Vac. Sci. Technol. A* **9**, 2331 (1991).
- ¹⁹N. Layadi, P. Roca i Cabarrocas, B. Drévillon, and I. Solomon, *Phys. Rev. B* **52**, 5136 (1995); *Solid State Phenom.* **37–38**, 281 (1994).
- ²⁰C. Godet, N. Layadi, and P. Roca i Cabarrocas, *Appl. Phys. Lett.* **66**, 3146 (1995).
- ²¹P. Roca i Cabarrocas, R. Cariou, and M. Labrune, *J. Non-Cryst. Solids* **358**, 2000 (2012).
- ²²E. V. Johnson, P. A. Delattre, and J. P. Booth, *Appl. Phys. Lett.* **100**, 133504 (2012).
- ²³D. Senouci, R. Baghdad, A. Belfedal, L. Shahed, X. Portier, S. Charvet, K. H. Kim, P. Roca i Cabarrocas, and K. Zellama, *Thin Solid Films* **522**, 186 (2012).
- ²⁴B. Yan, J. Yang, and S. Guha, *J. Vac. Sci. Technol. A* **30**, 04D108 (2012).
- ²⁵Q. Wang, I. Koleva, V. M. Donnelly, and D. J. Economou, *J. Phys. D: Appl. Phys.* **38**, 1690 (2005).
- ²⁶S. J. Kang and V. M. Donnelly, *Plasma Sources Sci. Technol.* **16**, 265 (2007).

- ²⁷The models and formalism used here appears in the J.A. Woollam, "Guide to Using WVASE32: Spectroscopic Ellipsometry Data Acquisition and Analysis Software," 2010. J.A. Woollam Co., Inc., Lincoln, NE. Similarly, the optical constants for crystal silicon and Aspnès amorphous silicon are available in file formats in WVASE32 software as *si_jaw.mat* and *a-si_aspnès.mat* and were used and reproduced here with the permission of the J.A. Woollam Co., Inc.
- ²⁸A. S. Ferlauto, G. M. Ferreira, J. M. Pearce, C. R. Wronski, R. W. Collins, X. Deng, and G. Ganguly, *J. Appl. Phys.* **92**, 2424 (2002).
- ²⁹See for example, P. Roca i Cabarrocas, N. Layadi, B. Drevillon, and I. Solomon, *J. Non-Cryst. Solids* **198–200**, 871 (1996).
- ³⁰T. Kaneko, K. Onisawa, M. Wakagi, Y. Kita, and T. Minemura, *Jpn. J. Appl. Phys.* **32**, 4907 (1993).
- ³¹L. Houben, M. Luysberg, P. Hapke, R. Carius, F. Finger, and H. Wagner, *Philos. Mag. A* **77**, 1447 (1998).
- ³²H. Xia, Y. L. He, L. C. Wang, W. Zhang, X. N. Liu, X. K. Zhang, D. Feng, and H. E. Jackson, *J. Appl. Phys.* **78**, 6705 (1995).
- ³³Q. Cheng, S. Xu, and K. Ostrikov, *Nanotechnology* **20**, 215606 (2009).
- ³⁴R. Tsu, J. Gonzales-Hernandez, S. S. Chao, S. C. Lee, and K. Tanaka, *Appl. Phys. Lett.* **40**, 534, (1982). In this reference, $y = 0.88$ was found for large grain poly-Si and $y = 0.08$ when using a single crystal silicon reference; E. Bustarret, M. A. Hachicha, and M. Brunel, *ibid.* **52**, 1675 (1988).
- ³⁵E. Vallat-Sauvin, C. Droz, F. Meillaud, J. Bailat, A. Shah, and C. Ballif, *J. Non-Cryst. Solids* **352**, 1200 (2006).
- ³⁶L. Ding, T. P. Chen, Y. Liu, C. Y. Ng, and S. Fung, *Phys. Rev. B* **72**, 125419 (2005).
- ³⁷Z. Iqbal and S. Veprek, *J. Phys. C* **15**, 377 (1982).
- ³⁸Ch. Ossadink, S. Veprek, and I. Gregora, *Thin Solid Films* **337**, 148 (1999).
- ³⁹H. S. Mavi, A. K. Shukla, S. C. Abbi, and K. P. Jain, *J. Appl. Phys.* **66**, 5322 (1989).
- ⁴⁰G.-X. Cheng, H. Xia, K.-J. Chen, W. Zhang, and X.-K. Zhang, *Phys. Status Solidi A* **118**, K51 (1990).
- ⁴¹S. Boultradakis, S. Logothetidis, S. Ves, and J. Kircher, *J. Appl. Phys.* **73**, 914 (1993).
- ⁴²A. Slaoui, F. Ehrhardt, F. Delachat, G. Ferbalntier, and D. Muller, *Proc. of SPIE* **8471**, 84710B-1 (2012).
- ⁴³I. Solomon, B. Drévilion, H. Shirai, and N. Layadi, *J. Non-Cryst. Solids* **164–166**, 989 (1993).
- ⁴⁴C. C. Tsai, G. B. Anderson, R. Thompson, and B. Wacker, *J. Non-Cryst. Solids* **114**, 151 (1989).
- ⁴⁵J. Perrin and J. F. M. Aarts, *Chem. Phys.* **80**, 351 (1983).
- ⁴⁶S. Agarwal, A. Takano, M. C. M. van de Sanden, D. Maroudas, and E. S. Aydil, *J. Chem. Phys.* **117**, 10805 (2002).
- ⁴⁷D. E. Carlson and C. W. Magee, *Appl. Phys. Lett.* **33**, 81 (1978).
- ⁴⁸A. E. Widmer, R. Fehlmann, and C. W. Magee, *J. Non-Cryst. Solids* **54**, 199 (1983).